The Astrophysical Journal Supplement Series, 266:21 (9pp), 2023 June https://doi.org/10.3847/1538-4365/acca75

A Dust Detection Database for the Inner Heliosphere Using the Parker Solar Probe Spacecraft

David M. Malaspina[1,2], Alexandru Toma[2,3], Jamey R. Szalay[4], Marc Pulupa[5], Petr Pokorný[6,7], Stuart D. Bale[5,8], and Keith Goetz[9]
[1] Astrophysical and Planetary Sciences Department, University of Colorado, Boulder, CO, USA; David.Malaspina@colorado.edu
[2] Laboratory for Atmospheric and Space Physics, University of Colorado, Boulder, CO, USA
[3] Physics Department, University of Colorado, Boulder, CO, USA
[4] Department of Astrophysical Sciences, Princeton University, Princeton, NJ, USA
[5] Space Sciences Laboratory, University of California, Berkeley, CA, USA
[6] NASA Goddard Spaceflight Center, Greenbelt, MD, USA
[7] The Catholic University of America, Department of Physics, Washington, DC, USA
[8] Physics Department, University of California, Berkeley, CA, USA
[9] School of Physics and Astronomy, University of Minnesota, Minneapolis, MN, USA
Received 2023 February 10; revised 2023 March 30; accepted 2023 April 3; published 2023 May 18

Abstract

A database of in situ dust impact detections made by the Parker Solar Probe spacecraft is created to facilitate studies of interplanetary dust dynamics in the inner heliosphere. A standardized dust detection methodology is established and tested for validity. Individual impact detections are included in the database, and are used to derive dust impact rates. Impact rates are corrected for effects related to high-amplitude plasma waves and undercounting due to finite detection window duration. These corrections suggest that: (i) most dust impacts on Parker Solar Probe are consistent with a random process; and (ii) the true dust impact rate may be ∼50% greater than the impact rate determined using uncorrected data for certain portions of the orbit, especially near perihelion.

Unified Astronomy Thesaurus concepts: Interplanetary dust (821); Solar wind (1534); Space vehicles (1549); Zodiacal cloud (1845); Astronomy databases (83)

1. Introduction

Populations of small dust grains (<1 mm) pervade interplanetary space, forming the interplanetary dust cloud. This material originates primarily from larger bodies, such as asteroids, comets, and Kuiper Belt objects, via breakup, disaggregation, sublimation, or collisional processes (Koschny et al. 2019). The trajectories of interplanetary dust grains are primarily determined by gravitation, radiation, electromagnetic forces, and collisions (Koschny et al. 2019).

While the interplanetary dust cloud spans the full breadth of the solar system, dust evolution is most dynamic in the inner heliosphere, sunward of 1 au. In this region, solar radiation and gravitational forces are most intense, and the higher dust cloud density substantially increases the probability of collisions (Dermott et al. 1984).

Remote-sensing observations of sunlight scattered by dust grains in the inner heliosphere, measured from locations between 0.3 and 1 au, are highly stable in time (Leinert et al. 1981; Stenborg et al. 2018). While individual dust grains are continually being created, destroyed, and passing through this region, this physics is averaged out in observations of light scattered by spatially diffuse dust. In situ observations of dust grains from spacecraft enable the trajectories (and therefore dynamic histories) of individual particles to be constrained (e.g., Grun et al. 1993; Baguhl et al. 1996; Altobelli et al. 2003, 2005, 2006, 2016). However, in situ observations are limited to only a few locations at any given time. A combination of remote-sensing observations (to capture the large-scale dust distribution structure) and in situ measurements (to resolve the trajectories of individual grains) allows both physical regimes to be observed.

Prior to 2018, the only in situ observations of interplanetary dust inside Mercury's orbit were made by the Helios A and B spacecraft (Krüger et al. 2020 and references therein), which launched in 1974 (A) and 1976 (B), and operated until 1985 (A) and 1979 (B). The perihelion distance of these spacecraft was 0.3 au.

The Parker Solar Probe (PSP) spacecraft (Fox et al. 2016) was launched in 2018 with the goal of exploring the inner heliosphere sunward of 0.3 au. Remote-sensing dust measurements from this spacecraft have resulted in important new progress being made in understanding near-Sun dust dynamics, by identifying long-hypothesized (Russell 1929) dust-depletion and dust-free zones (Stenborg et al. 2021, 2022).

While PSP does not carry a dedicated in situ dust detector instrument, dust impacts are detected using the FIELDS electric and magnetic field instrument (Bale et al. 2016). Dust detection via electric field instruments has been used on a large number of spacecraft where dedicated dust detection is unavailable (e.g., Gurnett et al. 1983, 1986; Laakso et al. 1989; Tsurutani et al. 2003; Meyer-Vernet et al. 2009; Zaslavsky et al. 2012; Malaspina et al. 2014; Andersson et al. 2015; Kellogg et al. 2016; Vaverka et al. 2019).

Dust grains traveling at high velocities (>1 km s^{-1}) relative to a spacecraft vaporize and ionize upon impact, creating a transient plasma cloud. This plasma cloud perturbs the electric potential near the spacecraft by several mechanisms (see Shen et al. 2021 and references therein): (i) electrons and ions in the impact plasma cloud escape the impact region with different velocities, creating a transient charge separation; (ii) a fraction of the electrons and ions in the plasma cloud are recollected by

spacecraft and antenna surfaces, altering their electric potential; and (iii) the electrostatic charge of the charge-separated expanding plasma cloud can induce potentials on spacecraft surfaces. Electric field sensors detect the superposition of these voltage perturbations, generally as high-amplitude ($\sim$10 to $>$1000 mV), impulsive (tens of microseconds) voltage spikes.

The electric potential perturbations generated by expanding plasma clouds can be detected many meters away from the impact site. In this way, nearly the entire spacecraft surface area becomes a sensitive collecting area for antenna-based dust observations (Page et al. 2020). This gives antenna dust detection the advantage of high count rates. PSP is bombarded by thousands of such impacts each orbit, creating a statistically robust data set of dust detections.

The PSP in situ dust data have revealed several novel aspects of interplanetary dust dynamics close to the Sun, including its spatial distribution (Malaspina et al. 2020; Page et al. 2020; Szalay et al. 2020), points of agreement and disagreement with predictive modeling (Szalay et al. 2021), estimates for the mass flux of the interplanetary dust ejected from the inner solar system (Szalay et al. 2021), localized collisional enhancements related to asteroid debris streams (Pusack et al. 2021; Szalay et al. 2021), and new understanding of the physics of spacecraft damage via dust impacts (Szalay et al. 2021; Malaspina et al. 2022). These studies have provided a new look at interplanetary dust dynamics in the inner heliosphere, but there is much to be learned, and many more discoveries are possible, especially as the PSP perihelion distance continues to decrease.

This work seeks to create a database of the dust impacts recorded by the PSP FIELDS instrument. The goal of this database is to facilitate future studies of the near-Sun interplanetary dust environment and to enable more direct comparisons between study results. To that end, a standardized dust detection methodology is established, along with impact rate estimates and a publicly accessible database of all in situ dust detections over the entire PSP mission.

The following section describes the FIELDS data sets used to create the dust database. Next, the detection algorithm is described and its accuracy quantified. Estimates of the dust rate, with corrections for dead time and undercounting, are then described. Uncertainties and caveats to the data set are discussed. Finally, the content and format of the database is described.

2. FIELDS Data

The PSP dust database is constructed using measurements made by the FIELDS instrument (Bale et al. 2016). FIELDS measures electric and magnetic fields in space using several sensors. This study makes use of data recorded by the four 2 m electric field antennas located in the plane of the spacecraft heat shield. There is a fifth electric field antenna mounted on the tail boom, but signals from that antenna are not used in this study.

Figure 1 shows the four electric field antennas used in this study (labeled as V_1, V_2, V_3, and V_4), as well as two unit vectors of the spacecraft body coordinate system. Spacecraft $+\hat{z}$ points along the long axis of the spacecraft out from the heat shield. During closest approach, $+\hat{z}$ is nearly parallel to the spacecraft–Sun line. Spacecraft $+\hat{x}$ points 90° away from spacecraft $\hat{z}$, toward the direction of orbital motion. During closest approach to the Sun, $+\hat{x}$ is nearly parallel to the spacecraft ram velocity vector. The spacecraft $+\hat{y}$ vector completes the orthogonal coordinate system and points approximately toward ecliptic south. Additional views of PSP and the FIELDS antenna configuration can be found in Bale et al. (2016) and Malaspina et al. (2016, 2020).

The FIELDS instrument uses several receivers to process data from the FIELDS electric and magnetic field sensors (Bale et al. 2016). The data sets generated by those receivers that are key to this work are described here.

The Time Domain Sampler (TDS) receiver measures signals from the FIELDS electric field antennas and the search coil magnetometer (SCM) with a bandpass from a few kHz to $\sim$1 MHz (Bale et al. 2016). Among other data products, the TDS records the maximum signed amplitude of the time-series data on a given channel each N seconds, as well as the rms value on that channel over those N seconds. The value of N is set by command, but is often set to $\sim$7 s sunward of 55 solar radii (R_S) and $\sim$55 s outside of 55 R_S. These data products are referred to in this work as TDSmax. The TDSmax sampling the V_2 FIELDS antenna monopole signal are used for in situ dust detection in this work.

The dust database is constructed using TDSmax data sampling the V_2 FIELDS antenna because V_2 is the only channel sampled by TDSmax at a regular cadence for all times during the PSP mission when the FIELDS instrument is powered on. Using other channels results in reduced coverage of time and radial distance.

The Digital Fields Broad (DFB) receiver on FIELDS (Malaspina et al. 2016) records signals from the FIELDS electric field antennas and the SCM in a bandpass from DC to 75 kHz. One of the DFB data products consists of high-cadence burst data. The burst data contain short intervals ($\sim 2^M \cdot 3.5$ s) of high-cadence ($150{,}000/2^M$ sample s^{-1}) time-domain electric and magnetic field data on six channels. The integer M is commandable in flight. It was set to 0 for most of the first six encounters, and to higher values during later encounters. DFB burst captures are continuously recorded, then undergo a competitive selection on board (Malaspina et al. 2016). The output of this competitive selection is a small number of captures that are written into the FIELDS onboard data storage at a rate of $\sim$1 capture/20 minutes. A subset of the recorded captures is sent to the ground, chosen by human-in-the-loop selection after each solar encounter. These data are referred to as DFB burst captures in this work.

A second DFB data product used in this study is the AC-coupled bandpass filter data (AC BPF). These data contain the peak absolute value amplitudes recorded each $\sim$0.87 s for seven time-domain signals with different bandpass content. In the AC BPF data, the lowest bandpass is centered near 879 Hz and the highest near 56.2 kHz. The higher-bandpass channels partially overlap with the TDS bandpass. The data used here sample the differential antenna channel $V_{34} = V_3 - V_4$. Data from this channel are used because V_{34} is configured as an input channel for the AC BPF data product for the largest fraction of the mission duration. Using other channels results in reduced time and radial distance coverage.

3. Dust Database

The intent of the PSP FIELDS dust database is to provide the community with standardized data products that capture, as accurately as possible, the dust impact count rate as well as the timing and characteristics of each detected impact.

Individual dust impacts are identified in the TDSmax data, and their characteristics are recorded (time of occurrence, peak

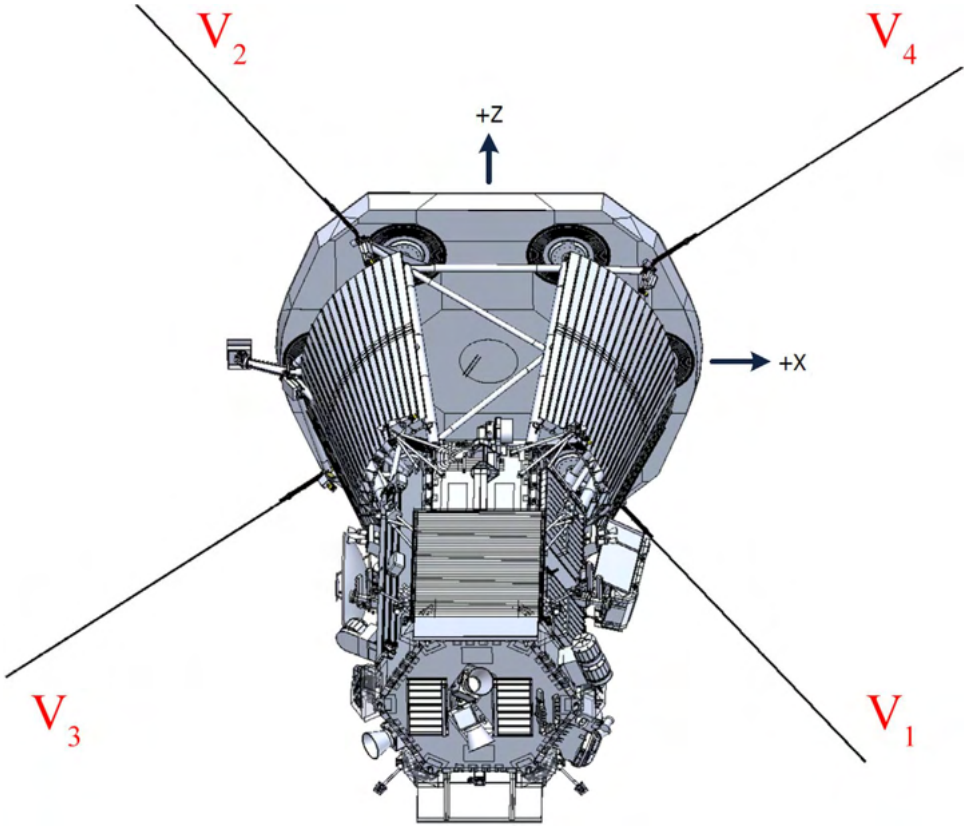

Figure 1. Mounting, orientation, and labels for the four FIELDS electric field antennas in the plane of the heat shield. This view does not include the tail boom where the FIELDS magnetic field sensors and the fifth electric field antenna are mounted. See Bale et al. (2016) for more detail on FIELDS.

signed amplitude, and rms value). Impact count rates are determined by summing the number of individual events within a specified time window and dividing by the number of seconds of valid data within that window. However, there are several issues that impact the accuracy of the impact identification and count rate determination. The methods implemented to address those issues are described here.

3.1. Dust Impact Identification in TDSmax Data

The characteristic shape of a time-domain voltage pulse created by a dust impact on PSP is well understood (Malaspina et al. 2020; Page et al. 2020). However, TDSmax data are not time-resolved. They return only one peak and rms value for each observation time window.

For the first few solar encounters, dust voltage pulses could be successfully separated from plasma waves in TDSmax data by setting an amplitude threshold. 50 mV was used in several studies (Malaspina et al. 2020; Page et al. 2020; Szalay et al. 2020; Pusack et al. 2021).

On encounter 8, and for all later encounters, PSP observed plasma waves that substantially exceed 50 mV in amplitude in the TDS frequency bandpass. These intervals primarily occur near perihelion, where the dust count rate is expected to be most dynamic.

Separating dust and plasma wave signals under these conditions requires examining both the peak and rms information for each event. Dust impact voltage signals are pulse-like, with a large peak/rms ratio. Plasma waves are often more sine-like, with a reduced peak/rms ratio.

Figure 2 shows two-dimensional histograms of TDSmax peak and rms values (a) for solar encounters 1–7, (b) for encounters 8–13, and (c) for encounters 1–13. Histograms of the column total and row total counts are shown below and to the right of each two-dimensional histogram. The horizontal black dashed lines show 50 mV. The angled black dashed line indicates peak/rms of 100.

Several regions of data are evident. Region 1 contains data with peak/rms > 100. Region 2 contains data with peak/rms < 100 and peak > 50 mV. Region 3 contains data with peak < 50 mV. For this dust database, the data in Region 1 are identified as dust impacts, the data in Region 2 are identified as high-amplitude plasma waves, and the data in Region 3 are identified as neither dust impacts nor high-amplitude waves. These regions are indicated in Figure 2(a) as R1, R2, and R3.

This method of dust impact identification relies only on peak and rms data, and therefore some events will inevitably be misidentified. To quantify the sorting accuracy, 100 randomly selected TDSmax times were chosen within each data region (using the encounter 1–13 data set). For each random time, AC BPF data recorded during the sample window of each random TDSmax sample (either ∼7 s or ∼55 s) were visually examined for signatures of a dust impact. Dust impacts appear as broadband signals in AC BPF data, with enhanced power across most or all bandpass bins at the time of the impact.

Region 1 is expected to contain primarily dust impacts. Of the random Region 1 times, AC BPF data showed dust signatures for 93, and no dust signatures for seven. Region 2 is expected to contain primarily high-amplitude plasma waves. Of the Region 2 random times, dust signatures were found for 16, and no dust signatures for 84. Region 3 is expected to contain

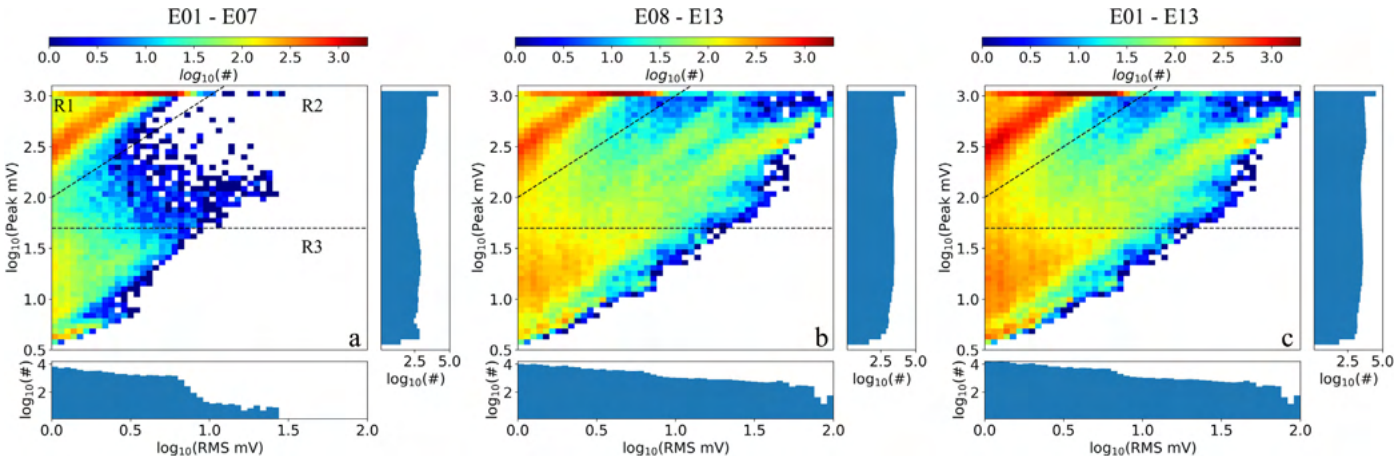

Figure 2. Two-dimensional histograms of TDSmax peak and rms values (a) for solar encounters 1–7, (b) for encounters 8–13, and (c) for encounters 1–13. Column total and row total histograms are shown to the bottom and right, respectively, of each two-dimensional histogram. See the text for descriptions of the regions R1, R2, and R3.

primarily signals other than dust. Of the Region 3 random times, dust signatures were found for five events, and no dust signatures for 95. From these randomly selected 300 times, the dust selection methodology employed yields a 93% true-positive rate, a 89.5% true-negative rate, a 10.5% false-positive rate, and a 7% false-negative rate.

The limitations of this validation method are important to consider. AC BPF data sampling a differential channel (V_{34}) is being compared with TDSmax data from the single-ended voltage measured by channel V_2. AC BPF data and TDSmax data have different (though partially overlapping) frequency bandpass ranges. However, there are mitigating factors that support this validation method. Most dust impacts create abrupt voltage pulses that span a broad range of frequencies, often spanning both the DFB and TDS bandpasses (Malaspina et al. 2020; Page et al. 2020). Also, dust impacts on PSP are often detected simultaneously by multiple antennas (Pusack et al. 2021). Finally, the solar probe antennas are physically short compared to the spacecraft size, with a geometrically asymmetric spacecraft between them, suggesting that differential voltage data and single-ended voltage data will have similar sensitivities for detecting impacts.

3.2. Dust Database: Individual Events

With these considerations, events included in the PSP/FIELDS dust impact database "individual impact" product must satisfy TDSmax peak/rms > 100 on the V_2 channel. All times of thruster firings and FIELDS antenna bias calibration sweeps (Bale et al. 2016) are removed from consideration. Dust impacts can only be identified in this way for times when the FIELDS instrument is powered on.

The dust database "individual impact" product contains the time corresponding to the center of the TDSmax window containing each impact, as well as the peak TDSmax voltage, rms TDSmax voltage, the distance of PSP from the Sun, the x, y, z location of PSP in ecliptic J2000 coordinates, and the solar encounter number.

3.3. Dust Database: Dust Impact Rates

Dust impact rates, in units of counts per hour, are also included in the PSP/FIELDS dust database. These data are calculated in three ways: (i) using directly observed counts and valid observation times ("raw"); (ii) using raw counts and observation times corrected for intense plasma wave intervals ("wave-corrected"); and (iii) using wave-corrected observation times and counts corrected for undercounting ("wave- and undercount-corrected").

The raw impact rate ($I_{\rm raw}$) is:

$$I_{\rm raw}(t_{\rm win}) = \frac{C_{\rm win}}{T_{\rm win}}, \quad (1)$$

where $t_{\rm win}$ is the center time of a given window (8 hr in duration), $C_{\rm win}$ is the number of dust impacts detected in that window, and $T_{\rm win}$ is the total time of the valid TDSMax observations in that window. Near perihelion, when FIELDS is continuously on, $T_{\rm win}$ is close to the full 8 hr window duration. Near aphelion, when FIELDS is often turned off to enable ground communication, $T_{\rm win}$ may be substantially smaller than the full window duration.

As discussed, plasma waves often reach high amplitudes near perihelion for encounter 8 and beyond. When this happens, dust impact signals can become small relative to plasma wave signals, and dust impacts will no longer be detectable using TDSmax peak and rms data alone. This decreases the total time of the possible dust impact observations. The wave-corrected impact rate ($I_{\rm wc}$) accounts for this wave-induced dead time:

$$I_{\rm wc}(t_{\rm win}) = \frac{C_{\rm win}}{T_{\rm win} - T_{\rm wav}}, \quad (2)$$

where $T_{\rm wav}$ is the total time when high-amplitude waves are present in the rate window. TDSmax observations that fall in Region 2 (Figure 2) are considered to be times of high-amplitude waves (peak/rms < 100, peak > 50 mV).

The third rate estimate included in the database also accounts for undercounting. Undercounting can occur because only one value of TDSmax peak and rms are reported each TDSmax time window, yet more than one dust impact may occur during a TDSmax time window. This is expected to occur more frequently close to the Sun where the count rates become high.

Figure 3 shows an example observation of three dust impacts that occur in a time span smaller than a typical TDSmax observation window ($\sim$7 s). Figure 3(a) shows DFB burst time-series data from two differential voltage channels (V_{12} and V_{34}).

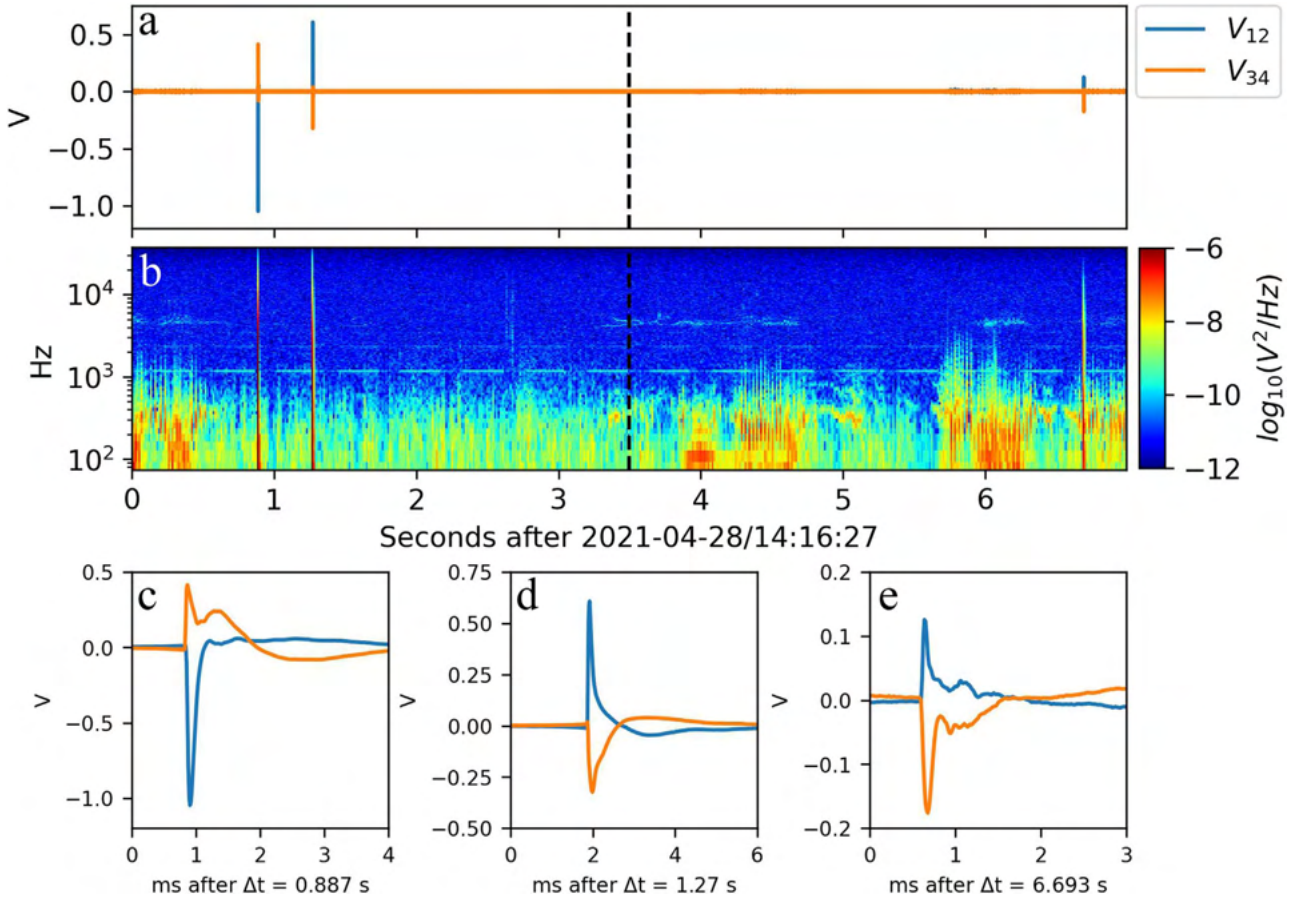

Figure 3. Example of a time-series burst data capture containing multiple dust impacts in less than 7 s. (a) Time series of differential voltage signals for channels V_{12} and V_{34}. (b) Spectrogram of the data in (a). (c)–(e) Details of the differential voltage signals from (a), showing time-series waveforms near each dust impact.

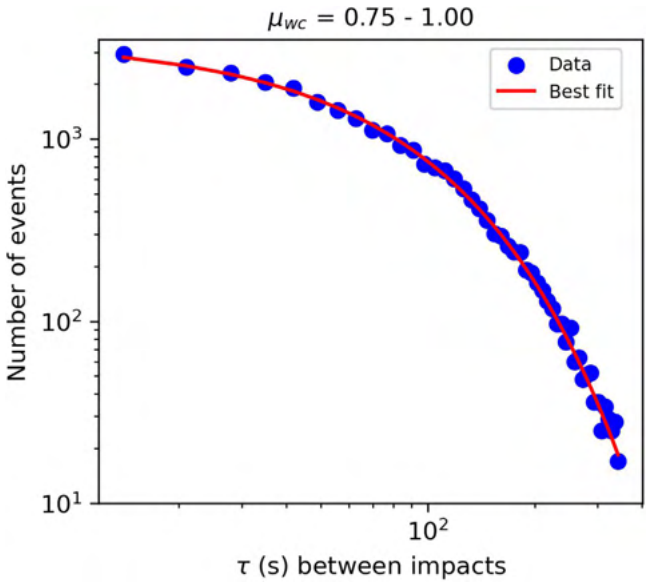

Figure 4. Distribution of measured waiting times between dust impacts, using all dust impacts recorded for Encounters 1 through 13 where the 8 hr impact rate was between 0.75 impacts minute^{-1} and 1.00 impacts minute^{-1}. The thin red lines shows a best-fit curve, using Equation (3) with $\mu_{corr} = 0.91$.

The abrupt spikes correspond to dust impacts. Figure 3(b) shows a spectrogram of the data in Figure 3(a). The dust impacts produce short-duration broadband pulses that are distinct from the other wave modes present. Figures 3(c), (d), and (e) show several milliseconds of differential voltage data near each impact. Each of the time-series shapes are consistent with prior observations of dust impacts on PSP (Malaspina et al. 2020; Page et al. 2020).

A waiting time analysis of the TDSmax data is used to estimate the extent of undercounting and correct the reported count rates for undercounting. First, each TDSmax dust detection from encounters 1 to 13 (Section 3.2) is assigned an impact rate (μ_{wc}) by interpolating the 8 hr wave-corrected impact rate (I_{wc}) to the time of each dust detection. Events are then sorted by μ_{wc} into 20 bins of width $\Delta\mu_{wc} = 0.25$ impacts minute^{-1}, spanning $\mu_{wc} = 0$ impacts minute^{-1} to $\mu_{wc} = 5$ impacts minute^{-1}. The waiting times between all events in a given μ_{wc} bin are calculated, and a histogram of waiting times is created for each bin. Each histogram uses 50 bins, evenly distributed in linear space between 0 s and 50 × 6.99 s, where 6.99 s is the time duration of the shortest TDSmax observation window used for encounters 1–13.

The following analysis assumes that the dust impacts on PSP detected by the TDSmax data product are randomly distributed in time (are not temporally clustered), and are well characterized by a single impact rate at any time when a similar value of I_{wc} is observed. Under these assumptions, the distribution of waiting times between impacts can be described as

$$f(\tau) = A(\mu_{corr}\tau)e^{-\mu_{corr}\tau}, \quad (3)$$

where A is a normalization constant, μ_{corr} is the undercount-corrected impact rate (impacts s^{-1}), and τ is the time between impacts.

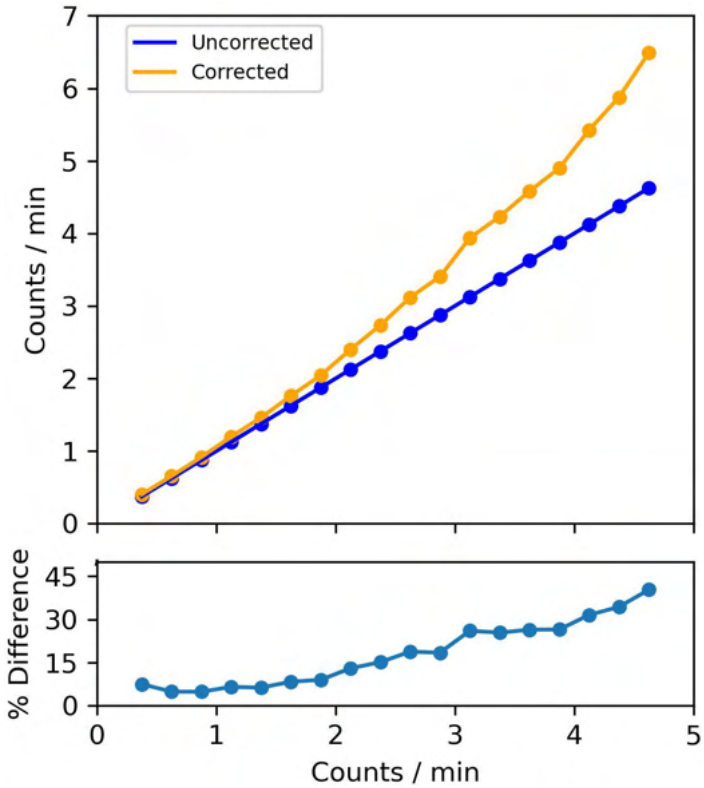

Figure 5. (Top) Impact rates corrected for undercounting, shown using the orange curve, as a function of impact rates not corrected for undercounting. A 1:1 line, representing no correction, is shown for comparison using the blue curve. (Bottom) The percentage difference between the corrected and uncorrected impact rates as a function of the uncorrected impact rate.

The waiting time distribution function for each μ_{wc} bin is fit using Equation (3) and a nonlinear least squares method, with μ_{corr} and A as fit parameters. μ_{wc} is used as the initial guess for μ_{corr} in the fitting routine, and A is an arbitrary amplitude.

Figure 4 shows the observed waiting time distribution of TDSmax events for the μ_{wc} bin spanning 0.75–1.00 impacts minute^{-1} (blue circles). The best-fit curve using Equation (3) is indicated by the red line, with $\mu_{corr} = 0.91$ impacts minute^{-1}.

The undercount-corrected impact rate is determined by fitting the waiting time distribution for each value of μ_{wc}. Figure 5 shows the fit-determined undercount-corrected impact rates (μ_{corr}) as a function of the uncorrected impact rates (μ_{wc}). A 1:1 line is shown for reference. The impact rate correction is small for low count rates, and increases at higher count rates, consistent with expectations that undercounting has a larger effect at higher impact rates.

Figure 6 illustrates the three impact rates reported by the PSP/FIELDS dust database: (i) the directly observed impact rate, I_{raw} (black solid line); (ii) the wave-corrected impact rate, I_{wc} (red dashed line); and (iii) the undercount-corrected impact rate, I_{ucc} (blue dotted line). Figure 6(a) shows seven days before and after perihelion for Encounter 10. Figure 6(b) shows the onboard-calculated AC-coupled electric field power spectra for this time interval. A seven-sample median filter is applied along the time axis to suppress individual dust impact spike signals in the spectral data, maximizing the visibility of the plasma wave activity. Noticeable corrections for plasma wave dead time are evident near perihelion, where high-amplitude broadband electric field signatures are present. Corrections for undercounting scale with the raw impact rate, as expected from the results in Figure 5.

4. Discussion

Based on the validity analysis presented in Figure 2, slightly more than ∼90% of the TDSmax dust identifications correspond to actual dust impacts. This leads to an inherent uncertainty on the order of ∼10% for any of the dust count rates derived using these data. Scientific conclusions drawn from the PSP dust database should therefore be robust to at least this level of uncertainty in order to be considered valid.

Several assumptions were made as part of the waiting time analysis to derive undercount corrections, including the assumption that dust impacts on PSP are a random process. Physically, this assumption is equivalent to assuming that the observed dust grains are not bunched spatially or temporally. Small-scale spatial or temporal bunching may be expected as a result of grain destruction caused by disaggregation or sputtering, which provide little momentum to separate newly detached grains. If the newly created grains are of similar size and shape, they are likely to experience similar forces and remain closely spaced. The smallest TDSmax data window (>7 s) used in this database may be too long to observe deviations from a random process due to closely spaced dust grains.

A second assumption used in the undercount correction process is that all observed dust impacts can be represented by a single impact rate. It is well established that at least two (e.g., Page et al. 2020; Szalay et al. 2021 and references therein), and possibly more (Pusack et al. 2021; Szalay et al. 2021), distinct

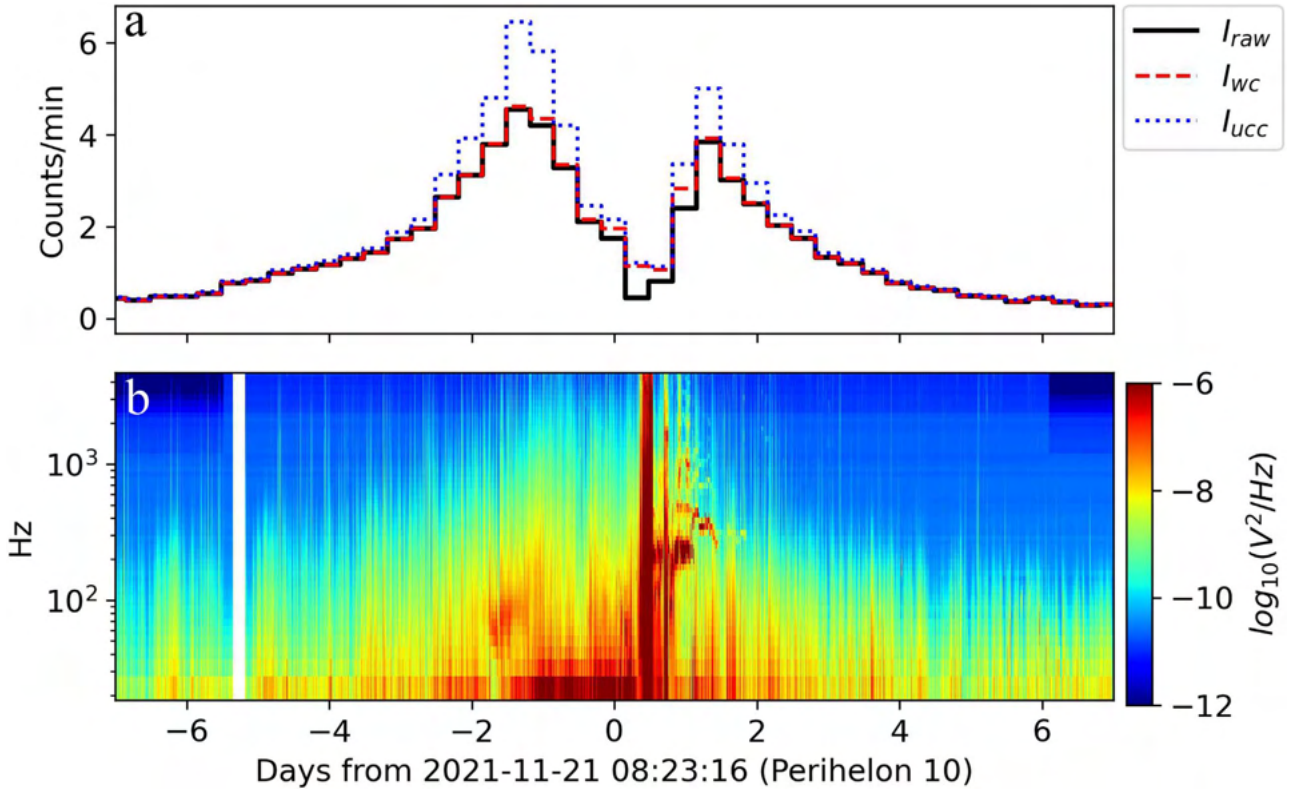

Figure 6. (a) Comparison of dust impact rates determined for Encounter 10, including directly measured (I_{raw}; black solid line), corrected for wave dead time (I_{wc}; red dashed line), and corrected for wave dead time and undercounting (I_{ucc}; blue dotted line). (b) Differential voltage power spectral density as a function of time, showing plasma wave activity during Encounter 10. See the text for details.

dust populations exist in the inner heliosphere. These populations are expected to have different spatial distributions and impact velocities, resulting in different impact rates on PSP. The analysis presented in this work treats only the aggregate waiting time distribution. In future work, taking into account separate populations may lead to more accurate estimates for the undercounting rate.

Another important consideration is that the sensitivity of FIELDS dust detection to dust grains of different masses varies throughout each orbit. The amount of charge released by a hypervelocity impact scales with the impact speed scaled to a large power (∼3.5 or ∼4; see Collette et al. 2014 and references therein). The impact speed is the relative velocity between a dust grain and the spacecraft, a quantity that is not uniform across dust grain mass or radial distance (Szalay et al. 2020). Therefore, the observed and corrected count rates are a convolution of the detection threshold, dust mass, dust velocity, and spacecraft velocity at each radial distance.

At the time of writing, PSP is nearing its fifteenth perihelion, of 25 planned. As the spacecraft continues to traverse unexplored regions of the heliosphere, it may become necessary to adjust the algorithms used here to compensate for unanticipated phenomena. This has occurred once already, during the transition from encounter 7 to encounter 8, described above, as plasma wave activity increased significantly. The reader seeking to use data from beyond encounter 14 is advised to look for additional release notes related to the FIELDS dust data product.

5. Conclusions

This study defines the data products that comprise the PSP FIELDS dust database. Descriptions of database variables are included in the supplemental material. A dust detection methodology using PSP FIELDS data was presented and its accuracy evaluated. Corrections to the raw count rate to account for the occurrence of high-amplitude plasma waves and undercounting due to finite observation time windows were derived and implemented. During this process, it was found that the dust impacts on the solar probe are, to first order, well described as a random process.

It is the authors' hope that this database expedites the work of researchers exploring the dynamics of interplanetary dust in the inner heliosphere. Finally, the authors intend to continually update the database as new data are returned from the PSP spacecraft.

Parker Solar Probe was designed, built, and is now operated by the Johns Hopkins Applied Physics Laboratory as part of NASA's Living with a Star (LWS) program (contract NNN06AA01C). Support from the LWS management and technical team has played a critical role in the success of the Parker Solar Probe mission. This effort was funded as part of NASA PSP Guest Investigator grant 80NSSC21K1764. All data used here, and the dust database data products, are publicly available on the FIELDS data archives: http://fields.ssl.berkeley.edu/data/.

Appendix
Data Product Description

The PSP dust database files are stored and archived in the FIELDS instrument data archives[10] as a Level 3 (L3) data product. As such, the dust database files follow the file organization and naming

[10] http://fields.ssl.berkeley.edu/data/

Table 1
Individual Impact Variables

Variable Name	Content
psp_fld_l3_dust_V2_event_peak_mV	Largest amplitude (signed) reported by TDSmax in the TDSmax window, in units of mV.
psp_fld_l3_dust_V2_event_rms_mV	Rms amplitude (signed) reported by TDSmax in the TDSmax window, in units of mV.

Table 2
Count Rate Variables

Variable Name	Content
psp_fld_l3_dust_V2_rate_raw	Dust impacts detected per second (see the primary text).
psp_fld_l3_dust_V2_rate_wav	Dust impacts detected per second, corrected for times where high-amplitude plasma waves inhibit dust detection (see the primary text).
psp_fld_l3_dust_V2_rate_ucc	Dust impacts detected per second, corrected for times where high-amplitude plasma waves inhibit dust detection, with corrections for undercounting applied (see the primary text).
psp_fld_l3_dust_V2_rate_ej2000_x	*X* position of the spacecraft in ecliptic J2000 coordinates, in units of solar radii.
psp_fld_l3_dust_V2_rate_ej2000_y	*Y* position of the spacecraft in ecliptic J2000 coordinates, in units of solar radii.
psp_fld_l3_dust_V2_rate_ej2000_z	*Z* position of the spacecraft in ecliptic J2000 coordinates, in units of solar radii.
psp_fld_l3_dust_V2_rate_dist_Rs	Radial distance of the spacecraft from the center of the Sun, in units of solar radii.
psp_fld_l3_dust_V2_rate_encounter	Solar encounter number.
psp_fld_l3_dust_V2_rate_inoutbound	Indicates the inbound (sunward) or outbound (antisunward) motion of the spacecraft during the data window.

Table 3
Spacecraft Attitude and Velocity Variables

Variable Name	Content
psp_fld_l3_dust_ej2000_pointing_velocity	Spacecraft velocity, in ecliptic j2000 coordinates and units of kilometers per second.
psp_fld_l3_dust_ej2000_pointing_sc_x_vector	Three-dimensional unit vector describing the attitude of the spacecraft *x*-axis in ecliptic j2000 coordinates. The spacecraft $+x$-axis is approximately parallel to the spacecraft ram direction when the spacecraft is near perihelion.
psp_fld_l3_dust_ej2000_pointing_sc_y_vector	Three-dimensional unit vector describing the attitude of the spacecraft *y*-axis in ecliptic j2000 coordinates. The spacecraft $+y$-axis is approximately parallel to the vector pointing normal to and south of the ecliptic plane when the spacecraft is near perihelion.
psp_fld_l3_dust_ej2000_pointing_sc_z_vector	Three-dimensional unit vector describing the attitude of the spacecraft *z*-axis in ecliptic j2000 coordinates. The spacecraft $+z$-axis is approximately parallel to the vector pointing from the spacecraft to the Sun when the spacecraft is near perihelion.

conventions used by other FIELDS data products. One file is produced for each day where one or more dust impacts are detected by the methodology described in the main article. This section describes each variable within the dust database files.

Each file contains data relevant to (i) individual dust impacts, (ii) impact rates, and (iii) ancillary information that is important for interpreting the dust impact data.

All data products have associated epoch time values included in the data file. Each epoch time value corresponds to the center time of each sample window.

Variables that contain data for individual dust impacts (events) are described in Table 1. These variables have irregular time cadences because they are only generated for TDSmax time windows where a dust impact is detected.

Variables that contain data for dust impact count rates (rates) are described in Table 2. These variables have a regular 8 hr time cadence. Position and epoch values are relevant to the center time of the 8 hr window.

Variables that contain data for spacecraft attitude and velocity (pointing) are described in Table 3. These variables have a regular 1 minute time cadence. Position and epoch values are relevant to the center time of the 1 minute window.

ORCID iDs

David M. Malaspina https://orcid.org/0000-0003-1191-1558
Alexandru Toma https://orcid.org/0000-0002-1831-1582
Jamey R. Szalay https://orcid.org/0000-0003-2685-9801
Marc Pulupa https://orcid.org/0000-0002-1573-7457
Petr Pokorný https://orcid.org/0000-0002-5667-9337
Stuart D. Bale https://orcid.org/0000-0002-1989-3596
Keith Goetz https://orcid.org/0000-0003-0420-3633

References

Altobelli, N., Grün, E., & Landgraf, M. 2006, A&A, 448, 243
Altobelli, N., Kempf, S., Krüger, H., et al. 2005, JGRA, 110, A07102
Altobelli, N., Kempf, S., Landgraf, M., et al. 2003, JGRA, 108, 8032
Altobelli, N., Postberg, F., Fiege, K., et al. 2016, Sci, 352, 312
Andersson, L., Weber, T. D., Malaspina, D., et al. 2015, Sci, 350, 0398
Baguhl, M., Grün, E., & Landgraf, M. 1996, SSRv, 78, 165
Bale, S. D., Goetz, K., Harvey, P. R., et al. 2016, SSRv, 204, 49
Collette, A., Grün, E., Malaspina, D., & Sternovsky, Z. 2014, JGRA, 119, 6019
Dermott, S. F., Nicholson, P. D., Burns, J. A., & Houck, J. R. 1984, Natur, 312, 505
Fox, N. J., Velli, M. C., Bale, S. D., et al. 2016, SSRv, 204, 7
Grun, E., Zook, H. A., Baguhl, M., et al. 1993, Natur, 362, 428
Gurnett, D. A., Averkamp, T. F., Scarf, F. L., & Grun, E. 1986, GeoRL, 13, 291

Gurnett, D. A., Grun, E., Gallagher, D., Kurth, W. S., & Scarf, F. L. 1983, Icar, 53, 236
Kellogg, P. J., Goetz, K., & Monson, S. J. 2016, JGRA, 121, 966
Koschny, D., Soja, R. H., Engrand, C., et al. 2019, SSRv, 215, 34
Krüger, H., Strub, P., Sommer, M., et al. 2020, A&A, 643, A96
Laakso, H., Grard, R., Pedersen, A., & Schwehm, G. 1989, AdSpR, 9, 269
Leinert, C., Richter, I., Pitz, E., & Planck, B. 1981, A&A, 103, 177
Malaspina, D. M., Andersson, L., Ergun, R. E., et al. 2014, GeoRL, 41, 5693
Malaspina, D. M., Ergun, R. E., Bolton, M., et al. 2016, JGRA, 121, 5088
Malaspina, D. M., Stenborg, G., Mehoke, D., et al. 2022, ApJ, 925, 27
Malaspina, D. M., Szalay, J. R., Pokorný, P., et al. 2020, ApJ, 892, 115
Meyer-Vernet, N., Maksimovic, M., Czechowski, A., et al. 2009, SoPh, 256, 463
Page, B., Bale, S., Bonnell, J. W., et al. 2020, ApJS, 246, 51
Pusack, A., Malaspina, D. M., Szalay, J. R., et al. 2021, PSJ, 2, 186
Russell, H. N. 1929, ApJ, 69, 49
Shen, M. M., Sternovsky, Z., Garzelli, A., & Malaspina, D. M. 2021, JGRA, 126, e29645
Stenborg, G., Howard, R. A., Hess, P., & Gallagher, B. 2021, A&A, 650, A28
Stenborg, G., Howard, R. A., & Stauffer, J. R. 2018, ApJ, 862, 168
Stenborg, G., Howard, R. A., Vourlidas, A., & Gallagher, B. 2022, ApJ, 932, 75
Szalay, J. R., Pokorný, P., Bale, S., et al. 2020, ApJS, 246, 27
Szalay, J. R., Pokorný, P., Malaspina, D. M., et al. 2021, PSJ, 2, 185
Tsurutani, B. T., Clay, D. R., Zhang, L. D., et al. 2003, GeoRL, 30, 2134
Vaverka, J., Pavlů, J., Nouzák, L., et al. 2019, JGRA, 124, 8179
Zaslavsky, A., Meyer-Vernet, N., Mann, I., et al. 2012, JGRA, 117, A05102